Direct imaging of valence orbitals using hard x-ray photoelectron spectroscopy

Daisuke Takegami,[1] Laurent Nicolaï,[2] Yuki Utsumi,[1,*] Anna Meléndez-Sans,[1] Daria A. Balatsky,[1,3]
Cariad-A. Knight,[1,3] Connor Dalton,[1,3] Shao-Lun Huang,[1,4] Chi-Sheng Chen,[1,5] Li Zhao,[1] Alexander C. Komarek,[1]
Yen-Fa Liao,[6] Ku-Ding Tsuei,[6] Ján Minár,[2,†] and Liu Hao Tjeng[1,‡]

[1]*Max Planck Institute for Chemical Physics of Solids, Nöthnitzer Straße 40, 01187 Dresden, Germany*
[2]*New Technologies-Research Center, University of West Bohemia, Univerzitni 8, 306 14 Pilsen, Czech Republic*
[3]*Department of Physics and Astronomy, University of British Columbia, Vancouver, British Columbia, Canada V6T 1Z1*
[4]*Department of Physics, National Tsing Hua University, Hsinchu 30013, Taiwan*
[5]*Department of Electrophysics, National Yang Ming Chiao Tung University, Hsinchu 30010, Taiwan*
[6]*National Synchrotron Radiation Research Center (NSRRC), 101 Hsin-Ann Road, 30076 Hsinchu, Taiwan*

It was hypothesized already more than 40 years ago that photoelectron spectroscopy should in principle be able to image atomic orbitals. If this can be made to work for orbitals in crystalline solids, one would have literally a different view on the electronic structure of a wide range of quantum materials. Here, we demonstrate how hard x-ray photoelectron spectroscopy can make direct images of the orbitals making up the band structure of our model system, ReO_3. The images are energy specific and enable us to unveil the role of each of those orbitals for the chemical bonding and the Fermi surface topology. The orbital image information is complementary to that from angle-resolved photoemission and thus completes the determination of the electronic structure of materials.

I. INTRODUCTION

Photoelectron spectroscopy is one of the most powerful experimental methods to study the electronic structure of crystalline materials [1]. The ability to detect band dispersions via angle-resolved photoelectron spectroscopy (ARPES) experiments has firmly demonstrated its value in the research fields of high-T_c superconductivity [2] and topological insulators [3]. More recently, the development of hard x-ray photoelectron spectroscopy (HAXPES), thanks to the availability of high-brilliance synchrotron radiation sources, opens new research opportunities related to the much increased probing depth [4]. Here, we utilize HAXPES to implement a long-sought and complementary aspect of photoelectron spectroscopy, namely, the ability to image the key orbitals that build up the valence band structure of crystalline solid state materials.

Already more than four decades ago, Goldberg, Fadley, and Kono [5,6] calculated the photoionization cross sections for atomic orbitals with fixed spatial orientation and found that the cross sections are exactly proportional to the probability distribution of the initial orbital when the experiment is carried out with the special geometry where the polarization of the light and the momentum of the measured photoelectrons are parallel. Figure 1(a) displays this geometry. By rotating the sample and measuring the orientation dependence, the experiment would have the potential to make a direct spatial image of the orbital that is occupied. The method is a real-space and calculation-free type of imaging and is to be distinguished from ARPES experiments in momentum space that aim to obtain the images via inverse Fourier transformations [7–11].

Several experimental studies in the distant [12] and more recent [8–11] past have been perceived as having used (explicitly or implicitly) the Goldberg, Fadley, and Kono prescription, but in fact they have not [5,13]. In the early case [12] the light was not even polarized, and in all cases so far [7–12] the light polarization and the direction of the measured out-going photoelectrons were not parallel, invalidating [5,13] the applied plane-wave final-state approximation. Indeed, the experimental geometry required by Goldberg, Fadley, and Kono is awkward in the sense that it does not allow for photoemission experiments in normal emission, which is standard for any (angle-resolved) photoelectron spectroscopy setup. It was therefore also concluded in a recent review that orientation-dependent experiments with parallel light polarization and photoelectron direction are still to be carried out [13]. Furthermore, what is valid for freestanding atoms in a Goldberg, Fadley, and Kono experiment may not be applicable for solids. Indeed, scattering of electrons is very strong in solids, resulting in, among other things, the much discussed pronounced photoelectron diffraction effects [14–16]. This obviously does considerably disturb the measurement.
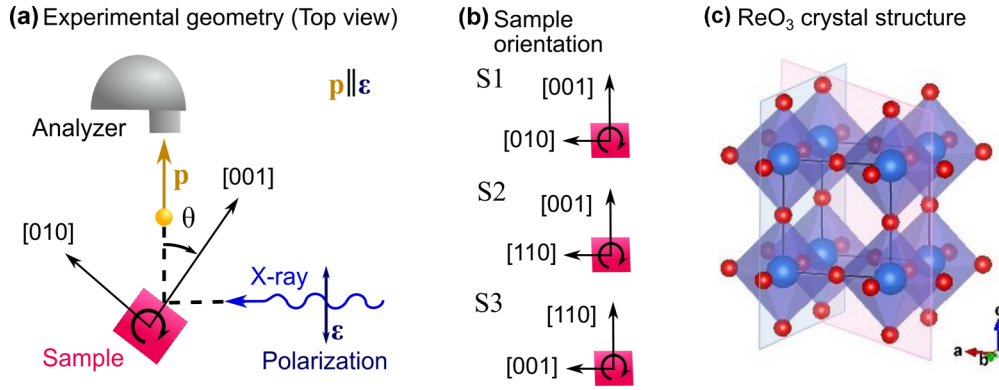

FIG. 1. (a) Top view of the experimental geometry of the hard x-ray photoelectron spectroscopy (HAXPES) experiment. The photoelectrons detected by the analyzer have their momentum **p** parallel to the electrical field ε of the x rays. θ is the polar angle. (b) Orientation of the three measured samples at $\theta = 0$ and their plane of rotation. (c) Crystal structure of ReO$_3$. Blue (red) spheres represent rhenium (oxygen) atoms. The blue (pink) plane corresponds to the plane of rotation for sample S1 (samples S2 and S3).

Here, we report our experimental and theoretical efforts to actually implement and prove the concept given by Goldberg, Fadley, and Kono for crystalline solids. If successful, we will be able to identify which of the atomic orbitals contribute to the valence band and, in particular, how they are oriented in the crystal and in which energy regions of the band structure. We will then have an energy-specific orbital imaging method which is purely experimental. This then will substantially advance our understanding of quantum materials and thus facilitate the search for new materials with new properties. As a model system we investigated ReO$_3$, an oxide with a simple but remarkable crystal structure, namely, a simple cubic arrangement of interconnected ReO$_6$ octahedra; see Fig. 1(c). In terms of properties, ReO$_3$ is an atypical and fascinating oxide: It is known as one of the best conducting oxides, with a conductivity comparable to that of Cu or Ag [17–20].

II. EXPERIMENT

ReO$_3$ single-crystal samples with three different orientations were used [Fig. 1(b)]. The rotation of the sample in the plane formed by **p** and the direction of the incoming photons is defined by the polar angle θ. The origin $\theta = 0°$ is set at the grazing incidence geometry, and the rotation direction is such that $\theta = 90°$ is at the normal incidence geometry. The experiments were performed in a range of $\theta = 1°$–$45°$. For sample S1, the crystal orientation at $\theta = 0°$ is [001], and at $\theta = 90°$ it is [010], defining the rotation plane corresponding to the blue cut in Fig. 1(c). In sample S2 (S3) the crystal orientation at $\theta = 0°$ is [001] ([110]), and at $\theta = 90°$ it is [110] ([001]), so that by using both samples the full $90°$ range between [001] and [110] can be measured. The rotation plane of these two samples corresponds to the pink cut in Fig. 1(c). We would like to note that by keeping the angle between the light polarization and the photoelectron direction the same throughout this sample-orientation-dependent study, we will not introduce intensity variations related to the asymmetry parameters in the photoionization cross section [21].

Figure 2(a) displays the HAXPES spectra of ReO$_3$ in their full measured range as a function of the orientation of the sample with respect to the electrical field ε of the photons. The

spectra shown here are from sample S1. The Re 4f core level is included in all measurements. The valence band spectra of all samples in all orientations are normalized against the Re 4f integrated intensity. Figure 2(c) provides a close-up of the valence region. We can observe three main features in these
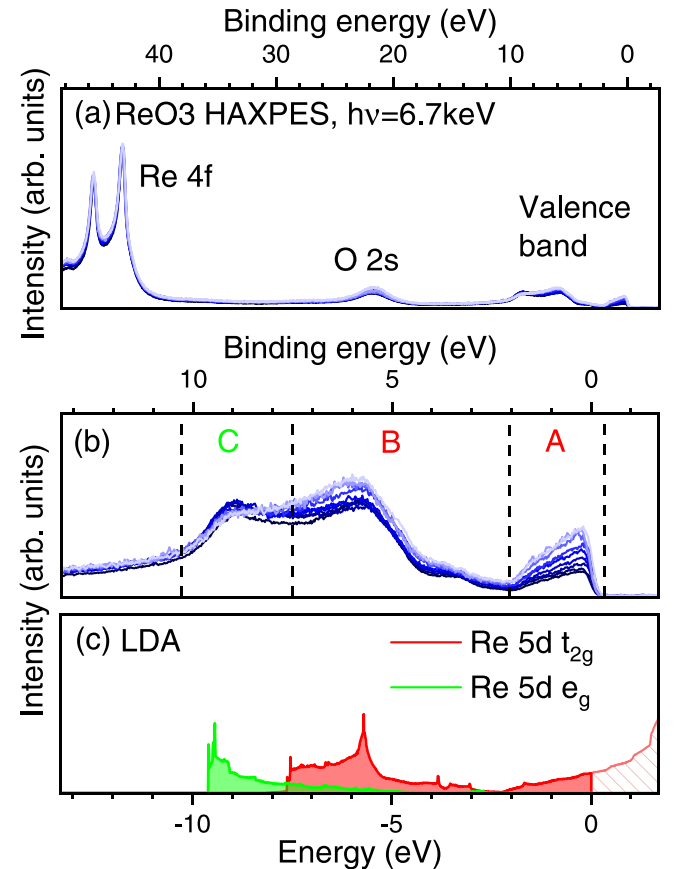

FIG. 2. (a) Experimental HAXPES spectra in their full measured range, normalized to the Re 4f core level intensity. The spectra displayed in this figure are from sample S1. (b) Close-up of the valence band. The valence band is divided into three regions: regions A, B, and C. (c) Calculated Re 5d t_{2g} and e_g partial density of states.
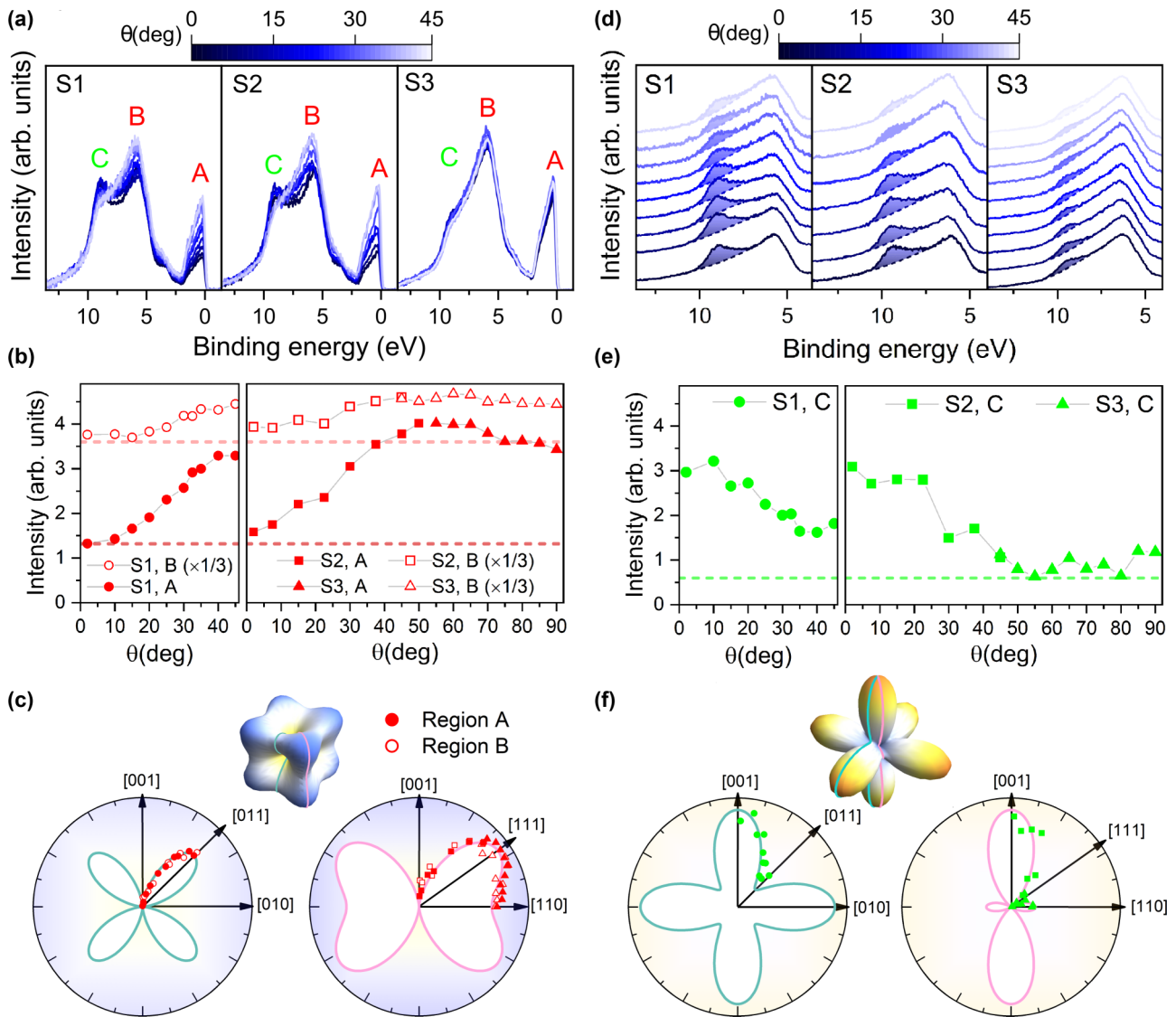
FIG. 3. (a) Valence band spectra of samples S1, S2, and S3 taken at different θ values. The experimental geometry is shown in Fig. 1, and the spectra have been normalized to the Re $4f$ core level and background subtracted. (b) Orientational dependence of the integrated intensity of regions A and B. The dashed lines represent the isotropic background used for the orbital analysis as described in the text. (c) Polar plots of the integrated intensities of regions A and B after the isotropic background subtraction, together with the theoretical atomic t_{2g} orbital. (d) Close-up of region C. The integrated intensity of the shaded area is used for the orbital analysis of the e_g states. (e) Orientational dependence of the integrated intensity of the shaded area in region C. The dashed lines represent the isotropic background used for the orbital analysis. (f) Polar plots of the integrated intensities of region C after the isotropic background subtraction, together with the theoretical atomic e_g orbital.

spectra. The first one is distributed in region A between 0 and 2 eV binding energy, the second is distributed in the wider region B between 2 and ≈ 7.5 eV, and the third is distributed in high-energy region C between ≈ 7.5 and ≈ 10.5 eV. We also can observe that the spectra depend on the orientation and that this orientation dependence is region specific.

III. ANALYSIS

To obtain a better view of the data, we have subtracted an integral type of background (known also as a "Shirley" background) from the spectra. In Fig. 3(a) we plot the results of all three samples measured at different values of the polar angle θ following the experimental geometry as displayed in

Fig. 1. Again, we can observe the very clear variations in the spectra as a function of the orientation of the sample with respect to the electrical field vector ε of the light. The sign and magnitude of the variations depend very much on the region, i.e., region A, B, or C.

To carry out the analysis more quantitatively, we first focus on region A and make a plot of its intensity against the crystallographic orientation. The result is shown in Fig. 3(b) by the solid red circles (sample S1, region A), solid red squares (sample S2, region A), and solid red triangles (sample S3, region A). It is important to note that the intensities obtained from different samples at common orientations ([001] ($\theta = 0°$) for samples S1 and S2, [011] (45°) for sample S1, [110] (90°) for sample S3, and [111] (55°) in the sample S2-S3 cut)

are consistent with each other. Furthermore, we can observe the minimum in the [001] (0°) direction, a maximum in the [011] (45°) direction on the cut defined by the geometry in sample S1 [left panel of Fig. 3(b)], the global maximum in the [111] (55°) direction, and a shallow minimum in the [110] (90°) on the cut defined by the geometry in sample S3 [right panel of Fig. 3(b)]. The positions of these maxima and minima correspond to those of the atomic t_{2g} orbital as displayed in Fig. 3(c), suggesting that there is a strong contribution of t_{2g} character in region A. However, we notice that we have a nonzero intensity in the minimum for the [001] (0°) direction.

We attribute this nonzero intensity to scattering processes that the emitted photoelectrons are enduring. We now take the ansatz that these processes are isotropic and will look later into whether this starting point can be *a posteriori* justified by the results and/or by calculations. We then take the nonzero value of the intensity observed in the [001] direction as the amount of isotropic background generated by these scattering processes. This background is indicated by the constant red dashed lines in Fig. 3(b). Subsequently, we subtract this background from the measured data and display the result with solid symbols in the polar plots of Fig. 3(c). We can observe that the background-corrected experimental data from region A fall accurately on top of the theoretical t_{2g} orbital shape.

Next we move our attention to region B. A plot of its intensity is shown in Fig. 3(b) by the open red circles (sample S1, region B), open red squares (sample S2, region B), and open red triangles (sample S3, region B). Similar to the data from region A, we can observe the minimum in the [001] ($\theta = 0°$) direction, a maximum in the [011] (45°) direction on the cut defined by the geometry in sample S1 [left panel of Fig. 3(b)], the global maximum in the [111] (55°) direction, and a shallow minimum in the [110] (90°) direction on the cut defined by the geometry in sample S3 [right panel of Fig. 3(b)]. We note that the contrast between the maxima and minima is not as large as in the case of region A. Nevertheless, the positions of these maxima and minima correspond to those of the atomic t_{2g} orbital.

In analogy to the analysis for region A, we infer that also for region B, scattering processes play an important role, and in fact, a dominant role. Using the ansatz of isotropic scattering and taking the constant red dashed lines in Fig. 3(b) to represent the background signal generated by the scattering processes, we can plot the background-corrected data for region B. The results are shown by the open symbols in Fig. 3(c). We can observe that the experimental data from region B also follow closely the theoretical t_{2g} orbital shape.

In analyzing the data from region C, we notice that the orientation dependence of region B could also contribute since the inelastically scattered electrons from region B will enter region C. In order to isolate the contribution that originates from region C only, a baseline subtraction is performed, as depicted in Fig. 3(d). The baseline is defined by an interpolation using the data points in the vicinity of the main peak from region B (at around 6 eV) and points at high binding energies (at around 10 eV), where there is no orientation dependence present anymore. A cubic spline interpolation was performed to ensure a smooth curve. The dashed lines in Fig. 3(d) show this baseline. The spectral feature that is then used for the orbital analysis is indicated by the shaded area.

Figure 3(e) displays plots of the intensity of the shaded area in region C as a function of the orientation. The solid green circles, squares, and triangles are the data collected from samples S1, S2, and S3. In contrast to the plot from region A, we notice here a maximum in the [001] ($\theta = 0°$) direction, a minimum in the [011] (45°) direction on the cut defined by the geometry in sample S1 [left panel of Fig. 3(e)], the global minimum in the [111] (55°), and a small maximum in the [110] (90°) direction on the cut defined by the geometry in sample S3 [right panel of Fig. 3(e)]. The positions of these maxima and minima correspond well to those of the atomic e_g orbital as plotted in Fig. 3(f). Yet the agreement is not perfect, especially in the [111] (55°) direction, where the experiment shows a nonzero intensity whereas an e_g orbital has a node.

Subtracting an isotropic background as depicted by the dashed lines in Fig. 3(e), we can obtain a polar plot where the experimental data do match very satisfactorily with the theoretical shape of an atomic e_g orbital; see Fig. 3(f). The experimental data thus suggest the presence of e_g character in this energy region of the valence band.

IV. THEORETICAL VALIDATION

To substantiate our experimental findings, we performed *ab initio* band structure calculations with the full-potential local-orbital (FPLO) code [22]. Here, we take advantage of the recent finding that such calculations can explain well the ReO₃ Fermi surface and the dispersions of the bands as measured very recently by angle-resolved photoelectron spectroscopy (ARPES) [23]. In Fig. 2(c) we show the calculated partial density of states (DOS) of the Re 5d t_{2g} and e_g. These could serve as a direct comparison for our HAXPES spectra since the photoionization cross section at 6.7 keV photon energy for the Re 5d is orders of magnitude larger than that for the O 2p [21,24], so that the valence band HAXPES spectra of ReO₃ are basically reflecting primarily the Re 5d.

In Fig. 2(c) reveals that the Re 5d states in region A between 0 and 2 eV binding energy are of pure t_{2g} character, those in region B between 2 and 7.5 eV are of mainly t_{2g} character with some e_g character, and those in region C between 7.5 and 10.5 eV are of pure e_g character. The calculations thus provide full support for the character assignments that we have made based on the orbital images from the measurements for the respective regions.

To justify the analysis procedure that we have applied to the experimental data, we have performed *ab initio* photoemission calculations using the one-step model based on a local density approximation (LDA) fully relativistic layer Korringa-Kohn-Rostoker (KKR) formalism with a time-reversed low-energy electron diffraction (LEED) final state [25,26]. The one-step model furthermore fundamentally encompasses all geometry- and light-induced effects, such as the incidence angle or the light polarization. The calculations have been carried out for the specific experimental geometry used in this paper. The experimental photon energy of 6.7 keV, a sample temperature of 81 K, and a Debye temperature of 140 K were utilized in the calculations.

Figure 4(a) displays the calculated photoemission spectra for the sample S1 geometry. The spectra are normalized to the integrated intensity in the full Re 5d range, i.e., from −15
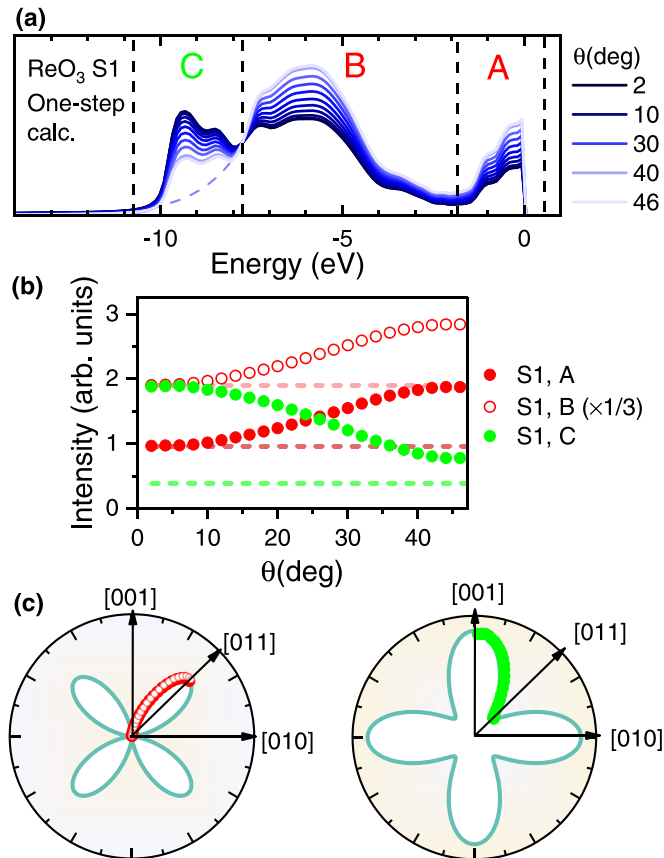
FIG. 4. (a) Calculated valence band spectra by using the one-step model in the experimental geometries corresponding to sample S1, after normalization to the total integrated intensity in the full Re $5d$ range. (b) Angular dependence of the integrated intensity of regions A, B, and C, following the same procedures as with the experimental spectra. (c) Polar plots after an isotropic background subtraction, together with the projections of the theoretical atomic t_{2g} (left panel) and e_g (right panel) orbitals.

to +10 eV [27]. A strong dependence on the orientation can be observed. Applying the same analysis procedure to these theoretical results that we used for the experimental data, we can obtain the integrated intensities of regions A, B, and C as a function of the angle θ. The results are shown in Fig. 4(b). We see quite similar angular profiles, as in the experiment, and we also see the presence of an isotropic background in the angular dependence. Subtracting the isotropic background as indicated by the dashed lines in Fig. 4(b), we can draw polar plots of the intensities as depicted in in Fig. 4(c). We can observe clearly that regions A and B consist of t_{2g} states and region C consists of e_g states.

What we can infer from the calculations is first of all that the orbital information is indeed contained in the spectra when the special geometry shown in Fig. 1 is being used for the experiment. The calculations and experimental results also demonstrate that the normalization procedures followed, namely, to use in the calculations the integrated signal of the spectra in the full Re $5d$ range and to use in the experiment a nearby shallow core level belonging to the same atomic emitter, are very effective in removing the otherwise

pronounced angular dependence due to x-ray photoelectron diffraction (XPD) processes [14–16]. As far as the experiment is concerned, we can infer that the shallow core levels and the valence band have very similar XPD effects related to the fact that they have practically the same kinetic energies [28]. Furthermore, fully filled cores have a spherical symmetry and thus do not display any initial-state orientation dependence. Therefore, by normalizing the spectra to the shallow core levels we can expect to normalize all effects except for those that depend on the initial-state orientation dependence of the partially filled valence band orbitals.

The calculations also show that we are in the so-called x-ray photoemission spectroscopy (XPS) limit where the ARPES-related features are washed out, yielding a more local atomiclike photoemission signal. This in turn also recovers the starting point of Goldberg, Fadley, and Kono [5,6] and thus allows for the method of orbital imaging to work. Yet elastic scattering and inelastic scattering of the photoelectrons are important and do add a background signal to the orientation dependence of the spectra. The calculations seem to suggest that this background signal is rather isotropic, thereby supporting or justifying the empirical approach of isotropic background subtraction that we have used to obtain the orbital images of ReO$_3$ from the measurements.

V. DISCUSSIONS AND CONCLUSION

Quantitative knowledge about the scattering processes is important especially for cases of mixed orbital occupation. For example, in the analysis of region B we have subtracted an isotropic background so as to yield only the t_{2g} orbital shape. This is obviously not quite correct since band structure calculations indicate that there should also be some (minor) contribution from the e_g states in region B. Indeed, since any $t_{2g} : e_g$ admixture in a 3 : 2 ratio produces a spherically shaped orbital, the subtraction of too much isotropic background has effectively removed the (weak) presence of the e_g. The ability to quantify the scattering background will therefore help in disentangling mixed orbital states. For completeness, we would like to mention that the spin-orbit interaction as well as atomic Coulomb and exchange interactions will also directly mix the t_{2g} and e_g states [29,30], but for ReO$_3$ with its large effective octahedral crystal field [31] this effect plays a minor role. Also our band structure calculations find, for example, that the amount of e_g character in the t_{2g}-like states near the Fermi level is not more than 1%.

Nevertheless, for systems with strong orbital polarization and for valence band states closest to the Fermi level which suffer the least from inelastic scattering processes, one could make use of this orbital imaging method without the need to do scattering calculations. The identification of the maxima and minima in the orientation dependence will already provide good indications of the type of the main orbital that is occupied and for its orientation within the crystal. This aspect is, in particular, attractive for strongly correlated materials [32–35], where band structure calculations are not reliable and the interpretation of ARPES data is complex.

As far as the ReO$_3$ system is concerned, we observed using the orbital imaging method that the states crossing the Fermi level originate from the atomic Re $5d$ t_{2g}. While this is also

found from our FPLO calculations, the assignment to such an orbital state from band structure calculations in general may vary depending on the basis functions used, although the calculated charge density and band structure are, or should be, basis independent. Our experimental observation is therefore a valuable confirmation that it is a useful starting point to think about the near-Fermi-level states of ReO$_3$ in terms of Re $5d$ t_{2g} orbitals. This in turn explains directly why the spin-orbit interaction in the Re $5d$ can indeed be active in shaping the topology of the Fermi surface [23]. This is related to the fact that t_{2g} states can be split by spin-orbit coupling, which is strong in the $5d$ elements, while by contrast, e_g states will remain unaffected [36].

The direct observation via orbital imaging of e_g states at the bottom of the valence band of ReO$_3$ provides also an important clue about the nature of the Re-O bonding. Although it is probably correct to state that the low-energy excitations of ReO$_3$ are primarily determined by the t_{2g} degrees of freedom, one cannot ignore the role of the e_g states in the formation of the material. This Re^{6+} oxide with the formal $t_{2g}^1 e_g^0$ configuration may have its e_g state at high energies due to the strong octahedral crystal field, but the measured presence of e_g electrons in the valence band is proof that the σ hybridization with the O $2p$ is very strong and thus significantly contributes to the cohesive energy of ReO$_3$.

Orbital imaging of the valence band therefore provides direct insight into the nature of chemical bonding and Fermi surface topology in quantum materials and complements the information gathered from band structure calculations and angle-resolved photoemission experiments.

APPENDIX: METHODOLOGY

The experiments have been carried out at the Max Planck–National Synchrotron Radiation Research Center (NSRRC) HAXPES end station at the Taiwan undulator beamline BL12XU at SPring-8, Japan. The photon beam was linearly polarized with the electrical field vector in the plane of the storage ring (i.e., horizontal), and the photon energy was set at about 6.7 keV. The overall energy resolution was set at 0.27 eV. The measurements were performed at 80 K. The analyzer is mounted parallel to the photon beam's electrical field ε as shown in Fig. 1(a). The momentum of the measured photoelectrons **p** is therefore also parallel to ε, as proposed by Goldberg, Fadley, and Kono [5,6].

The one-step model of photoemission is implemented in the spin-polarized relativistic Korringa-Kohn-Rostoker (SPR-KKR) scheme of the Munich band structure software package, based on Green's function and multiple-scattering spin-density matrix formalisms [25,26]. The LDA has been chosen to approximate the exchange-correlation part of the potential. The bulk potential is converged within the atomic sphere approximation geometry, and we have used an experimental lattice constant of 3.79 Å. We used an angular momentum expansion up to a $l_{max} = 3$. The accuracy of all approximations has been cross-checked by detailed comparison with the FPLO results. After self-consistency was reached, the ARPES calculations were performed and are based on the one-step model of photoemission in its spin density matrix formulation using the same geometry as used in the experiments. This theory accounts for effects induced by the light polarization, matrix-element effects, final-state effects, and surface effects. Lifetime effects in the final states have been simulated via a constant imaginary part $V_{0f} = 12$ eV in the inner potential, and the lifetime of the initial state was simulated by an imaginary part of $V_{0i} = 0.15$ eV. It is important to note that in order to obtain direct imaging of valence orbitals, the so called the x-ray photoemission spectroscopy (XPS) limit in the HAXPES has to be utilized. In particular, even at very low temperatures (tenths of a kelvin), indirect (nonconserving momentum **p**) transitions occur [28,37]. The corresponding averaging over the Brillouin zone leads to density-of-states-like spectra for any emission angle. This effect we took into account by the so-called alloy analogy model, where atomic displacements are averaged by coherent potential approximation [38]. The temperature-dependent displacements were estimated from the Debye temperature.

[1] S. Hüfner, *Photoelectron Spectroscopy: Principles and Applications*, Advanced Texts in Physics (Springer, Berlin, 2003).

[2] A. Damascelli, Z. Hussain, and Z.-X. Shen, Angle-resolved photoemission studies of the cuprate superconductors, Rev. Mod. Phys. **75**, 473 (2003).

[3] M. Z. Hasan and J. E. Moore, Three-dimensional topological insulators, Annu. Rev. Condens. Matter Phys. **2**, 55 (2011).

[4] *Hard X-ray Photoelectron Spectroscopy (HAXPES)*, edited by J. C. Woicik, Springer Series in Surface Sciences (Springer, Cham, Switzerland, 2016), Vol. 59.

[5] S. M. Goldberg, C. S. Fadley, and S. Kono, Photoelectric cross-sections for fixed-orientation atomic orbitals: Relationship to the plane-wave final state approximation and angle-resolved photoemission, Solid State Commun. **28**, 459 (1978).

[6] S. M. Goldberg, C. S. Fadley, and S. Kono, Photoionization cross-sections for atomic orbitals with random and fixed spatial orientation, J. Electron Spectrosc. Relat. Phenom. **21**, 285 (1981).

[7] M. Månsson, T. Claesson, M. Finazzi, C. Dallera, N. B. Brookes, and O. Tjernberg, Using High Energy Angle Resolved

Photoelectron Spectroscopy to Reveal the Charge Density in Solids, Phys. Rev. Lett. **101**, 226404 (2008).

[8] P. Puschnig, S. Berkebile, A. J. Fleming, G. Koller, K. Emtsev, T. Seyller, J. D. Riley, C. Ambrosch-Draxl, F. P. Netzer, and M. G. Ramsey, Reconstruction of molecular orbital densities from photoemission data, Science **326**, 702 (2009).

[9] W. S. Jung, C. S. Leem, C. Kim, S. R. Park, S. Y. Park, B. J. Kim, E. Rotenberg, and C. Kim, Imaging the electron density in solids by using multi-Brillouin-zone angle resolved photoelectron spectroscopy, Phys. Rev. B **82**, 235105 (2010).

[10] S. Weiß, D. Lüftner, T. Ules, E. M. Reinisch, H. Kaser, A. Gottwald, M. Richter, S. Soubatch, G. Koller, M. G. Ramsey, F. S. Tautz, and P. Puschnig, Exploring three-dimensional orbital imaging with energy-dependent photoemission tomography, Nat. Commun. **6**, 8287 (2015).

[11] P. Kliuiev, G. Zamborlini, M. Jugovac, Y. Gurdal, K. von Arx, K. Waltar, S. Schnidrig, R. Alberto, M. Iannuzzi, V. Feyer, M. Hengsberger, J. Osterwalder, and L. Castiglioni, Combined orbital tomography study of multi-configurational molecular adsorbate systems, Nat. Commun. **10**, 5255 (2019).

[12] F. R. McFeely, J. Stöhr, G. Apai, P. S. Wehner, and D. A. Shirley, d-orbital-directed photoemission from silver and gold, Phys. Rev. B **14**, 3273 (1976).

[13] A. M. Bradshaw and D. P. Woodruff, Molecular orbital tomography for adsorbed molecules: is a correct description of the final state really unimportant?, New J. Phys. **17**, 013033 (2015).

[14] C. S. Fadley, M. A. Van Hove, Z. Hussain, and A. P. Kaduwela, Photoelectron diffraction: new dimensions in space, time, and spin, J. Electron Spectrosc. Relat. Phenom. **75**, 273 (1995).

[15] C. S. Fadley, X-ray photoelectron spectroscopy and diffraction in the hard x-ray regime: Fundamental considerations and future possibilities, Nucl. Instrum. Methods Phys. Res., Sect. A **547**, 24 (2005).

[16] G. Schönhense, K. Medjanik, S. Babenkov, D. Vasilyev, M. Ellguth, O. Fedchenko, S. Chernov, B. Schönhense, and H.-J. Elmers, Momentum-transfer model of valence-band photoelectron diffraction, Commun. Phys. **3**, 45 (2020).

[17] A. Ferretti, D. B. Rogers, and J. B. Goodenough, The relation of the electrical conductivity in single crystals of rhenium trioxide to the conductivities of Sr_2MgReO_6 and Na_xWO_3, J. Phys. Chem. Solids **26**, 2007 (1965).

[18] C. N. King, H. C. Kirsch, and T. H. Geballe, The low temperature heat capacity and electrical resistivity of ReO_3, Solid State Commun. **9**, 907 (1971).

[19] T. P. Pearsall and C. A. Lee, Electronic transport in ReO_3: dc conductivity and Hall effect, Phys. Rev. B **10**, 2190 (1974).

[20] T. Tanaka, T. Akahane, E. Bannai, S. Kawai, N. Tsuda, and Y. Ishizawa, Role of polar optical phonon scattering in electrical resistivities of LaB_6 and ReO_3, J. Phys. C: Solid State Phys. **9**, 1235 (1976).

[21] M. B. Trzhaskovskaya, V. K. Nikulin, V. I. Nefedov, and V. G. Yarzhemsky, Non-dipole second order parameters of the photoelectron angular distribution for elements $Z = 1–100$ in the photoelectron energy range 1–10 keV, At. Data Nucl. Data Tables **92**, 245 (2006).

[22] K. Koepernik and H. Eschrig, Full-potential nonorthogonal local-orbital minimum-basis band-structure scheme, Phys. Rev. B **59**, 1743 (1999).

[23] J. Falke, C. F. Chang, C. E. Liu, D. Takegami, A. Melendez-Sans, C.-S. Chen, L. Zhao, A. C. Komarek, C.-Y. Kuo, C. T. Chen, and L. H. Tjeng, Electronic structure of the metallic oxide ReO_3, Phys. Rev. B **103**, 115125 (2021).

[24] D. Takegami, D. Kasinathan, K. K. Wolff, S. G. Altendorf, C. F. Chang, K. Hoefer, A. Melendez-Sans, Y. Utsumi, F. Meneghin, T. D. Ha, C. H. Yen, K. Chen, C. Y. Kuo, Y. F. Liao, K. D. Tsuei, R. Morrow, S. Wurmehl, B. Büchner, B. E. Prasad, M. Jansen *et al.*, Charge-transfer energy in iridates: A hard x-ray photoelectron spectroscopy study, Phys. Rev. B **102**, 045119 (2020).

[25] H. Ebert, D. Ködderitzsch, and J. Minár, Calculating condensed matter properties using the KKR-Green's function method – recent developments and applications, Rep. Prog. Phys. **74**, 096501 (2011).

[26] J. Braun, J. Minár, and H. Ebert, Correlation, temperature and disorder: Recent developments in the one-step description of angle-resolved photoemission, Phys. Rep. **740**, 1 (2018).

[27] The calculations were normalized by integrating over the full range of the Re $5d$ both below and above the Fermi level so as to obtain the intensity of a full shell on the Re site, analogous to the use of the full-shell Re $4f$ in the experiment.

[28] A. X. Gray, C. Papp, S. Ueda, B. Balke, Y. Yamashita, L. Plucinski, J. Minár, J. Braun, E. R. Ylvisaker, C. M. Schneider, W. E. Pickett, H. Ebert, K. Kobayashi, and C. S. Fadley, Probing bulk electronic structure with hard x-ray angle-resolved photoemission, Nat. Mater. **10**, 759 (2011).

[29] S. Agrestini, C.-Y. Kuo, K.-T. Ko, Z. Hu, D. Kasinathan, H. B. Vasili, J. Herrero-Martin, S. M. Valvidares, E. Pellegrin, L.-Y. Jang, A. Henschel, M. Schmidt, A. Tanaka, and L. H. Tjeng, Electronically highly cubic conditions for Ru in $\alpha-RuCl_3$, Phys. Rev. B **96**, 161107(R) (2017).

[30] G. L. Stamokostas and G. A. Fiete, Mixing of $t_{2g} - e_g$ orbitals in $4d$ and $5d$ transition metal oxides, Phys. Rev. B **97**, 085150 (2018).

[31] L. F. Mattheiss, Band Structure and Fermi Surface of ReO_3, Phys. Rev. **181**, 987 (1969).

[32] R. J. Cava, Oxide superconductors, J. Am. Ceram. Soc. **83**, 5 (2000).

[33] D. I. Khomskii, *Transition Metal Compounds* (Cambridge University Press, Cambridge, 2014).

[34] B. Keimer, S. A. Kivelson, M. R. Norman, S. Uchida, and J. Zaanen, From quantum matter to high-temperature superconductivity in copper oxides, Nature (London) **518**, 179 (2015).

[35] S. Wirth and F. Steglich, Exploring heavy fermions from macroscopic to microscopic length scales, Nat. Rev. Mater. **1**, 16051 (2016).

[36] See Fig. 4 of Ref. [31].

[37] A. X. Gray, J. Minár, S. Ueda, P. R. Stone, Y. Yamashita, J. Fujii, J. Braun, L. Plucinski, C. M. Schneider, G. Panaccione, H. Ebert, O. D. Dubon, K. Kobayashi, and C. S. Fadley, Bulk electronic structure of the dilute magnetic semiconductor $Ga_{1-x}Mn_xAs$ through hard X-ray angle-resolved photoemission, Nat. Mater. **11**, 957 (2012).

[38] J. Minár, J. Braun, and H. Ebert, Recent developments in the theory of HARPES, J. Electron Spectrosc. Relat. Phenom. **190**, 159 (2013).